IEEE Access
Multidisciplinary | Rapid Review | Open Access Journal

Received December 11, 2019, accepted December 17, 2019, date of publication December 23, 2019,
date of current version January 2, 2020.

Digital Object Identifier 10.1109/ACCESS.2019.2961373

Error Analysis and Correction of a Downhole Rotating Magnetic Full-Tensor Gradiometer

YANGYI SUI[1], (Member, IEEE), WEI HE[1], ZHENGHUI XIA[1], SHIBIN LIU[1], AND KEITH LESLIE[2]

[1]Key Laboratory of Geo-Exploration Instruments, College of Instrumentation and Electrical Engineering, Ministry of Education of China, Jilin University, Changchun 130026, China
[2]CSIRO Manufacturing, Lindfield, NSW 2070, Australia

Corresponding author: Yangyi Sui (suiyangyi@jlu.edu.cn)

This work was supported in part by the National Natural Science Foundation of China under Grant 41574174, and in part by the National Key Research and Development Program of China under Grant 2018YFC1503903.

ABSTRACT Compared with ground magnetic measurement and aeromagnetic survey, downhole magnetic measurements can provide more abundant and accurate distribution information of ore deposits. Measurement of the full magnetic tensor gradient affords more information than either traditional magnetic total field or three, orthogonal axes, vector field measurements. Gradient field measurements are less influenced by any time and/or spatial changes of the Earth's magnetic field during the measurement period. CSIRO has developed the world first downhole magnetic full tensor gradiometer and carried out field tests. This gradiometer is based on a rotation of two fluxgate vector field sensors to enable frequency separation of the common mode from the gradient signals. Reposition of the gradiometer about three, nominally orthogonal axes, enables measurement of the full gradient tensor with one pair of fluxgate sensors. This paper describes a method to improve the accuracy of this type of gradiometer. System errors have been analyzed and classified according to the effect of the errors on the measurement accuracy. Major errors include scale factor error of the two fluxgates, misalignment and motion errors of these two sensors relative to the model system, and transformation errors when moving from the sensor to the instrument coordinate frame of reference. Minor errors include errors of finite length measurement parameters, errors associated with ignoring high-order tensors, the deviation of the rotation axis from ideal, and the temperature co-efficient of the fluxgates' signals. We have developed the error models for the major errors and calibrated the full-tensor gradiometer by using the two independent tensor rotation invariants. 1000 simulations with random errors show the root mean squares of relative error are less than 8% after calibration. The calibration technique was applied to field trail measurements made using a gradiometer that was re-oriented multiple times around a fixed point while measuring a known gradient. Applying the calibration method resulted in an improvement of the tensor magnitude accuracy by a factor of 3.74. This result validated the calibration method.

INDEX TERMS Downhole measurement, error analysis, invariant calibration, magnetic tensor gradiometer, rotating modulation.

I. INTRODUCTION

Large scale, total field, airborne and ground-based geophysical magnetic surveys are routinely used for the detection, localization and characterization (DLC) of magnetic targets [1]. Such surveys are undertaken both in the iron ore industry and in the non-ferrous minerals sector for determining the distribution of copper, nickel, chromium, diamonds [2]. In these surveys the signal to noise ratio (SNR) of any magnetic anomaly is influenced both by the sensor sensitivity and the separation between the sensor system and the anomaly. For ground based or airborne surveys, the minimum achievable separation is dictated by physical constraints which may result in a low SNR. Another limitation of any total field survey is the inability to detect magnetic anomalies with special structures whose magnetic potential is constant [3], for example a uniformly magnetized slab [4]. By contrast, when deploying a down-hole magnetic sensor, there is a potential to

The associate editor coordinating the review of this manuscript and approving it for publication was Giambattista Gruosso.

enhance the SNR due to the closer proximity between sensor and target and also the potential for determining more detailed structural information about the target by measuring three, nominally orthogonal, vector field components [5]. While it is common for downhole instruments to include vector magnetometers, the measured signals are highly dependent on the orientation of the probe with respect to the Earth's magnetic field, thus leading to difficulties in interpreting the vector measurements [2]. These difficulties can be overcome by measuring the magnetic field gradients [6].

Measurement of the gradients of the three orthogonal magnetic field components [7] is becoming a powerful technique for adding value to geophysical surveys. Compared with the total magnetic field and three-component magnetic vector measurements, the magnetic full tensor gradient measurement can provide more information [8] and is less influenced by the temporal and spatial changes of the Earth's magnetic field [9]. It also has the advantage of relative insensitivity to orientation errors [10].

The three main methods used for measuring the magnetic gradient tensor are [11]: First-order Taylor series approximation [12], rotation modulation [13], and string vibration [14]. First-order Taylor series approximation seems suitable for a full-tensor SQUID gradiometer system with a small baseline, but it cannot be applied practically in a downhole environment because of the requirement for cryogenic cooling and the limited space available inside the drill hole. The string vibration method can only measure partial components of magnetic gradient tensor and it is difficult to combine multiple modules inside a drill hole to enable a full tensor measurement.

The rotation modulation method separates the different derivatives of a magnetic scalar potential through rotating sensors to obtain second-order gradient tensor components. The DC and low-frequency performance of the instrument is not limited by the performance of the sensors and the gradiometer imbalance [15] is no longer directly determined by the engineering precision [13]. CSIRO has developed the world first downhole magnetic full tensor gradiometer using two fluxgates based on the principle of rotation modulation [2].

To further improve the measurement accuracy of the tensor gradiometer, the system errors have been analyzed and classified according to the effect of errors. Major errors include scale factor errors of the two fluxgate magnetometers, misalignment and motion errors of these two sensors relative to the model system, and errors that occur when transforming from sensor coordinates to the instrument frame of reference. Minor errors considered are errors due to the finite length of the measurement, errors due to ignoring high-order tensors, errors due to mechanical deviation of the rotation axis, and temperature drift. We have developed the error models for major errors and calibrated the full-tensor gradiometer by using the two independent tensor rotation invariants. The correctness of the calibration method was initially verified by simulation experiments and then by a field experiment in an area with a low gradient, magnetic field.

II. PRINCIPLE OF MEASUREMENT AND PROPAGATION OF ERROR

A. PRINCIPLE OF MEASUREMENT

The core idea of the rotation modulation method is to convert the signal in the spatial domain into the time domain through rotating magnetic sensors, to transform the measurement into the frequency domain using a Fourier Transform thus enabling separation of the different order magnetic gradient tensors by frequency selection.

Assume that $\boldsymbol{B}$ denotes the magnetic field vector, with three components B_x, B_y, and B_z. Define the centre point of the gradiometer as the origin. The Taylor series about the origin of a function $B(x, y, z)$ is

$$B(x,y,z) = \sum_{n=0}^{\infty} \frac{1}{n!} \left(x\frac{\partial}{\partial x} + y\frac{\partial}{\partial y} + z\frac{\partial}{\partial z} \right)^n B(\mathbf{0}) \quad (1)$$

Accordingly, three components of the magnetic field $B_\alpha(\boldsymbol{r})$ at the point $\boldsymbol{r}$ can be derived from $B_\alpha(\mathbf{0})$.

$$\begin{aligned} B_\alpha(\boldsymbol{r}) = B_\alpha(\mathbf{0}) &+ \left(x\frac{\partial}{\partial x} + y\frac{\partial}{\partial y} + z\frac{\partial}{\partial z} \right) B_\alpha \\ &+ \frac{1}{2!} \left(x\frac{\partial}{\partial x} + y\frac{\partial}{\partial y} + z\frac{\partial}{\partial z} \right)^2 B_\alpha \\ &+ \frac{1}{3!} \left(x\frac{\partial}{\partial x} + y\frac{\partial}{\partial y} + z\frac{\partial}{\partial z} \right)^3 B_\alpha + \cdots \end{aligned} \quad (2)$$

where $\alpha = x$, y, and z. $B_{\alpha x} = \partial B_\alpha / \partial x$, $B_{\alpha y} = \partial B_\alpha / \partial y$, $B_{\alpha z} = \partial B_\alpha / \partial z$ are the second derivatives of the magnetic scalar potential. Similarly, $B_{\alpha xx}$ denotes the components of the third-order gradient tensor.

When α takes x, y, and z respectively, we can get nine components of second-order tensor which can be expressed by

$$\boldsymbol{G} = \begin{bmatrix} \frac{\partial B_x}{\partial x} & \frac{\partial B_x}{\partial y} & \frac{\partial B_x}{\partial z} \\ \frac{\partial B_y}{\partial x} & \frac{\partial B_y}{\partial y} & \frac{\partial B_y}{\partial z} \\ \frac{\partial B_z}{\partial x} & \frac{\partial B_z}{\partial y} & \frac{\partial B_z}{\partial z} \end{bmatrix} = \begin{bmatrix} g_{xx} & g_{xy} & g_{xz} \\ g_{yx} & g_{yy} & g_{yz} \\ g_{zx} & g_{zy} & g_{zz} \end{bmatrix}. \quad (3)$$

Only five components of $\boldsymbol{G}$ are independent because the divergence and curl of the magnetic field are equal to zero in source-free regions [4]. $\boldsymbol{G}$ can be rewritten as

$$\boldsymbol{G} = \begin{bmatrix} g_{xx} & g_{xy} & g_{xz} \\ g_{xy} & g_{yy} & g_{yz} \\ g_{xz} & g_{yz} & -g_{xx} - g_{yy} \end{bmatrix}. \quad (4)$$

A magnetic full-tensor gradiometer can measure all these five independent components.

If we ignore the third- and higher order of the magnetic gradient tensor due to the fact that higher-order gradients fall

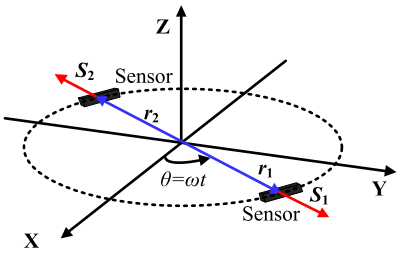

FIGURE 1. Schematic of two magnetic vector sensors, S_1 and S_2 placed at two points r_1 and r_2, relative to the origin of the coordinate system, and which rotate about the Z-axis with angular velocity ω.

off more rapidly with distance than lower-order ones, and only consider the x-y plane, (2) can be simplified to

$$B_\alpha(\boldsymbol{r}) \doteqdot B_\alpha(\mathbf{0}) + xg_{\alpha x} + yg_{\alpha y} = B_\alpha(\mathbf{0}) + \boldsymbol{g_\alpha} \cdot \boldsymbol{r}. \quad (5)$$

where g_α denotes the vector $(g_{\alpha x}, g_{\alpha y})$. Therefore, the differences in the magnetic field components at two points are

$$B_\alpha(\boldsymbol{r_1}) - B_\alpha(\boldsymbol{r_2}) \doteqdot \boldsymbol{g_\alpha} \cdot (\boldsymbol{r_1} - \boldsymbol{r_2}). \quad (6)$$

That means the second-order tensor can be obtained according to the magnetic fields measured by the sensors. In the rotating modulation method, two magnetic vector sensors are placed at two points $\boldsymbol{r}_1$ and $\boldsymbol{r}_2$ relative to the origin of the coordinate system, called the *sensor coordinate system*, tangentially to a circle of radius ρ, and rotate about a Z-axis with angular frequency ω, as shown in FIG. 1.

Magnetic sensitivity vectors and position vectors of the two sensors are respectively expressed by

$$\boldsymbol{S_1} = S_1(\cos\theta, \sin\theta), \quad \boldsymbol{S_2} = -S_2(\cos\theta, \sin\theta). \quad (7)$$
$$\boldsymbol{r_1} = \rho(cos\theta, sin\theta), \quad \boldsymbol{r_2} = -\rho(cos\theta, sin\theta). \quad (8)$$

According to (5), the magnetic fields at the points of the sensors can be respectively expressed by

$$B_\alpha(\boldsymbol{r_1}) \doteqdot B_\alpha(0,0) + \rho g_{\alpha x}\cos\theta + \rho g_{\alpha y} sin\theta. \quad (9)$$
$$B_\alpha(\boldsymbol{r_2}) \doteqdot B_\alpha(0,0) - \rho g_{\alpha x}\cos\theta - \rho g_{\alpha y} sin\theta. \quad (10)$$

The sensor output voltage can be expressed by

$$V = [\boldsymbol{S_1} \cdot \boldsymbol{B}(\boldsymbol{r_1}) + \boldsymbol{S_2} \cdot \boldsymbol{B}(\boldsymbol{r_2})]. \quad (11)$$

where $\boldsymbol{B}(\boldsymbol{r}_1)$ and $\boldsymbol{B}(\boldsymbol{r}_2)$ are the components of the magnetic field vector in the direction of the sensitive axis of the fluxgate sensor [13].

The output voltage is also a function of time due to the rotation of the sensors in an arbitrary magnetic field. After combining the trigonometric functions, expanding, and collecting harmonics, the output voltage is

$$V = V_0 + \sum_{n=1}^{\infty} [V_{ne}\cos(n\omega t) + V_{no}\sin(n\omega t)]. \quad (12)$$

where V_0 is the dc term, and V_{ne} and V_{no} are the magnitudes of the real part and the imaginary part of the nth harmonic of the rotation frequency, obtained from the Fourier transform of the output voltage V, respectively.

In (12) the coefficients

$$V_{1e} \doteqdot \varsigma_v B_x \quad (13)$$
$$V_{1o} \doteqdot \varsigma_v B_y \quad (14)$$
$$V_{2e} \doteqdot \xi_v (g_{xx} - g_{yy}) \quad (15)$$
$$V_{2o} \doteqdot 2\xi_v g_{xy}. \quad (16)$$

where

$$\xi_v = \frac{1}{2}\rho(S_1 + S_2), \varsigma_v = (S_1 - S_2). \quad (17)$$

Similarly, when sensors are re-oriented to rotate about the X-axis and the Y-axis, four more equations for second-order tensor components can be obtained.

$$U_{2e} \doteqdot \xi_u(g_{zz} - g_{xx}), \quad U_{2o} \doteqdot 2\xi_u g_{xz},$$
$$W_{2e} \doteqdot \xi_w(g_{yy} - g_{zz}), \quad W_{2o} \doteqdot 2\xi_w g_{yz}. \quad (18)$$

The diagonal tensor components can be solved by

$$g_{xx} \doteqdot \frac{V_{2e}}{3\xi_v} - \frac{U_{2e}}{3\xi_u}, \quad g_{yy} \doteqdot \frac{W_{2e}}{3\xi_w} - \frac{V_{2e}}{3\xi_v}, \quad g_{zz} \doteqdot \frac{U_{2e}}{3\xi_u} - \frac{W_{2e}}{3\xi_w}. \quad (19)$$

Accordingly, the full tensor can be expressed by

$$\boldsymbol{G} = \begin{bmatrix} \frac{V_{2e}}{3\xi_v} - \frac{U_{2e}}{3\xi_u} & \frac{V_{2o}}{2\xi_v} & \frac{U_{2o}}{2\xi_u} \\ \frac{V_{2o}}{2\xi_v} & \frac{W_{2e}}{3\xi_w} - \frac{V_{2e}}{3\xi_v} & \frac{W_{2o}}{2\xi_w} \\ \frac{U_{2o}}{2\xi_u} & \frac{W_{2o}}{2\xi_w} & \frac{U_{2e}}{3\xi_u} - \frac{W_{2e}}{3\xi_w} \end{bmatrix}. \quad (20)$$

However, as there was insufficient space within the downhole probe to accommodate three gradiometers rotating simultaneously about three orthogonal axes, the mechanical design was configured to enable a pair of rotating sensors to measure the full magnetic gradient tensor as is shown in FIG. 2.

The main idea is to meet the limitation of space at the expense of time. We rotate the sensors on a disk into three different sensor coordinate systems, C^i (i = 1, 2, and 3) in sequence. The equations in sensor coordinates are transformed to a common instrument coordinate system, C, and solved to yield the magnetic gradient tensor in C, which is called *data extraction*. The X-Y plane is defined by the base of the instrument. The Z-axis is normal to the X-Y plane and forms an axis of symmetry for the instrument in the sense that the azimuths of spin axes for the three sensor coordinate systems are distributed about the instrument's Z-axis. The three different sensor coordinate systems are obtained by rotating to angles of 0°, 120°, and 240° about the instrument Z-axis respectively and tilting the X-Y plane through an angle 35.2° to form an orthogonal set of C^i axes. Design consideration may dictate a choice of tilt angle other than 35.2° [16]. For all angles other than those close to 0°, the system design is capable of measuring the full magnetic gradient tensor.

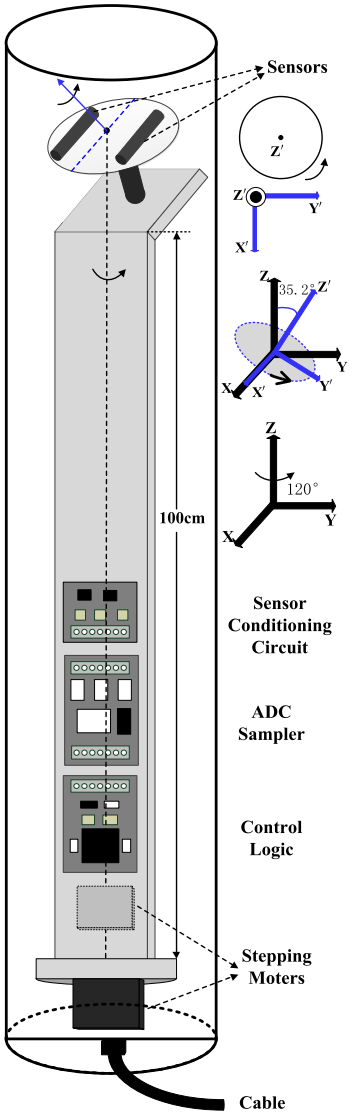

FIGURE 2. Schematic of the mechanical structure and rotation principle. There are two modes of rotations about two axes: one mode is rotation about the Z-axis through discrete 120° increments and the other is continuous rotation about the Z′-axis. The optimal angle between Z′- and Z-axis is 35.2°. The angle of rotation of the two sensors about the Z′ axis is measured using an optical shaft encoder.

III. PROPAGATION OF ERROR

The measurement process of the downhole tensor gradiometer includes four steps, shown in FIG. 3. Each step contributes different types of measurement errors that then propagate to the following steps. At the final step their overall combination limits the accuracy of the measurement of the magnetic gradient tensor components relative to the instrument coordinate system. The functions of each step and their relevant errors are described as follows:

Step 1: Rotate the magnetic sensors into three sensor coordinate systems and measure the magnetic field signals when rotating about Z'-axis with angular frequency ω. Errors in this step are the two individual fluxgate scale factor errors, non-zero offsets, temperature induced change in their sensitivities

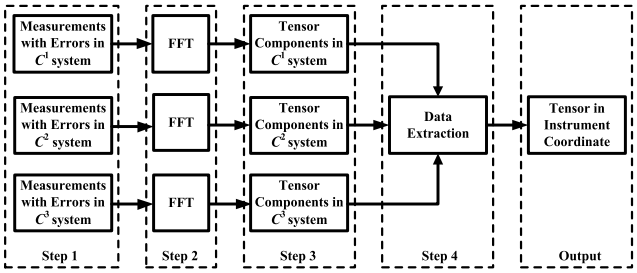

FIGURE 3. Schematic of propagation of error. The measurement process is divided into four steps. The first three steps describe the measurement in a single sensor coordinate system, including rotation of the sensor system into one of the three discrete positions 0°, 120° or 240°, see FIG 6(a), transforming time domain single into frequency domain signal by FFT, and calculating the magnetic gradient components, relative to the single sensor coordinate. The final step is to determine the full magnetic gradient tensor, relative to the instrument coordinate system, from the three sets of gradient components measured with respect to their individual sensor coordinates.

and positional errors in the sensor coordinate system such as misalignment of the fluxgates from ideal positioning and any offset of the rotation center.

Step 2: Transform the time domain signal into the frequency domain by a Fast Fourier Transform (FFT). The errors in this step are determined by the number of samples per rotation of the two sensors and the number of rotations per FFT.

Step 3: Solve the magnetic gradient tensor in the single sensor coordinate system one by one using (13) - (16). The errors in this step are that higher order terms are ignored when extracting the real and imaginary parts.

Step 4: Solve the magnetic gradient tensor in the instrument coordinate system C by transforming between the C^i and C systems using linear equations. Errors in this step include angle errors when rotating into C^i systems, and any mechanical installation error that results in non-overlapping of the Z-axis origins for three orientations of the sensor system as described in FIG 6 (a).

The errors are classified into major and minor errors and analyzed respectively.

IV. ANALYSIS AND MODELING FOR MAJOR ERRORS

A. ERROR MECHANISMS AND REPRESENTATIONS

1) FOR SCALE FACTOR ERROR

Magnetic sensors with the same specifications may not have exactly the same sensitivity, which means that two sensors may have slightly different output voltages in an identical magnetic field; this can be described as a scale factor error. FIG. 4 shows the equivalent schematic of the scale factor error in the downhole magnetic tensor gradiometer.

2) MISALIGNMENT ERRORS WITH RESPECT TO THE MODEL SYSTEM

There are two kinds of installation errors in a sensor coordinate system. One is misalignment of sensors, which makes the sensors non-tangential to the disk and leads to changes of

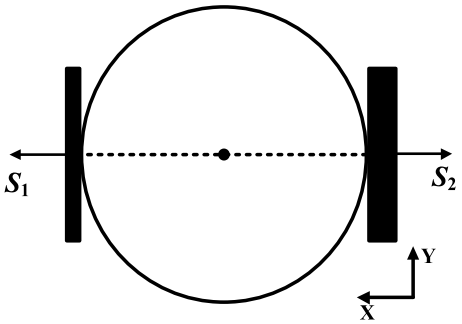

FIGURE 4. Schematic of scale factor error in the downhole magnetic tensor gradiometer. Differing scale factors are represented by the different sizes of the tangentially mounted sensors.

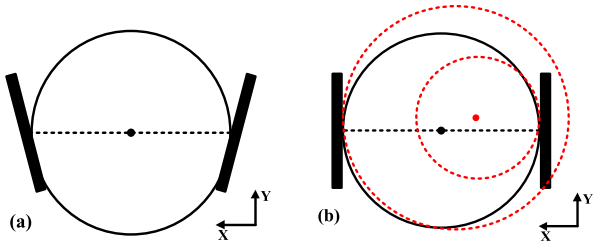

FIGURE 5. (a) Schematic of misalignment of sensors. The ideal sensor positions are tangential to the black solid line. (b) Schematic of offset between the rotation center and the center of the disk. The black dot is the ideal rotation center and the red dot is the actual rotation center. The red dashed lines are the actual motion tracks of two sensors.

the directions of the magnetic sensitivity vectors. The other is the offset between the rotation center and the center of the disk, which makes the two sensors asymmetric to the rotation center and affects the motion tracks of two sensors and the directions of the magnetic sensitivity vectors. FIG. 5 shows schematically the two types of installation errors.

3) FOR DATA EXTRACTION

The axis about which the two sensors are rotated is optimally tilted at an angle, λ, of 35.2° with respect to the overall system's Z-axis, see FIG 6 (b). Re-orientation of the sensor system about the Z-axis in three increments of 120°, FIG 6 (a), will then generate an orthogonal set of axes that allows measurement of the full tensor with just one set of rotating sensors. Manufacturing constraints introduce offsets in the accuracy of the 120° re-orientations and in the angle λ. Provided that these angular offsets are constant variations over repeated measurement cycles they can be corrected by system calibration. Any variation of these offsets from one measurement cycle to the next will impact on the accuracy of the determination of the tensor components.

B. ERROR MECHANISMS AND REPRESENTATIONS

1) FOR SCALE FACTOR ERROR

Considering the scale factor error and zero offset, the error model can be expressed by

$$B_M = SB_R + E. \tag{21}$$

where B_M is the measured value of the magnetic sensor, B_R is the true magnetic field, S denotes the scale factor, and E denotes the near static, non-zero offset of the magnetic sensor. Extraction of the gradient signal using frequency domain filtering of the sensor signal, ensures that the offset term is excluded from the measurement of gradient.

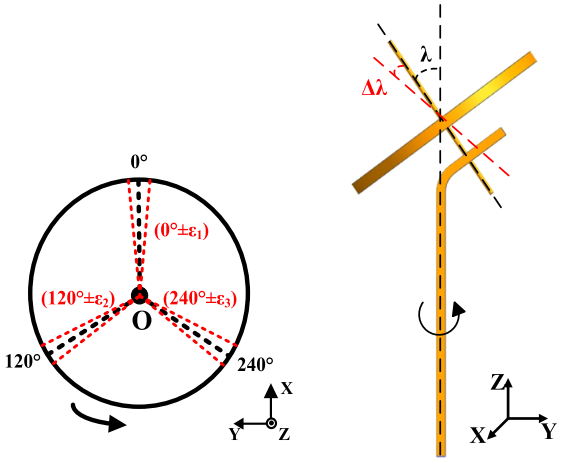

FIGURE 6. (a) The rotation angles about Z-axis are 0°, 120° and 240° with a small angle error ε_i, respectively. (b) The rotation angle about Y-axis is 35.2° with a small angle error Δλ.

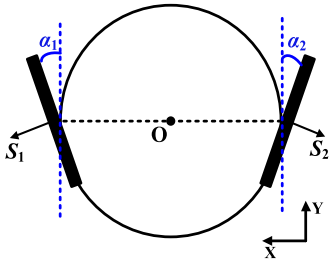

FIGURE 7. Schematic of the misalignment of two sensors. α_1 and α_2 are angles that sensors deviate from the Y-axis. The blue dashed lines represent the ideal locations of sensors.

2) MISALIGNMENT ERRORS

First, assume that the misalignment of two sensors leads two error angle α_1 and α_2, which are very small and generally within 3°. The magnetic sensitivity vectors of the two sensors in the sensor coordinate system can be expressed by

$$\begin{aligned} \boldsymbol{S_1} &= S_1 cos\,\alpha_1\,(cos\theta, sin\theta) \\ \boldsymbol{S_2} &= -S_2 cos\,\alpha_2\,(cos\theta, sin\theta). \end{aligned} \tag{22}$$

Second, there is an offset between the rotation center and the center of the disk due to limited manufacturing precision. Therefore, the ideal coordinate origin O (0, 0) is shifted to the actual coordinate origin O' (x_0, y_0).

Let the ideal radius of the disk be ρ, so the positions of the two sensors change from $(\rho, 0)$ and $(-\rho, 0)$ in the ideal coordinate system to $(\rho + x_0, -y_0)$ and $(-\rho + x_0, -y_0)$ in the actual coordinate system, C_a. The actual rotation radii of the two sensors in C_a are

$$\rho_1 = \sqrt{(\rho + x_0)^2 + y_0^2}\ \rho_2 = \sqrt{(\rho - x_0)^2 + y_0^2}. \tag{23}$$

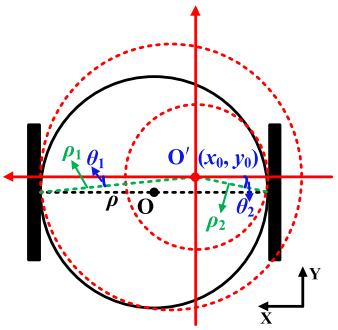

FIGURE 8. Schematic of the actual coordinate system with a red center. θ_1 and θ_2 are the actual starting angles, ρ_1 and ρ_2 are the actual rotation radii. ρ is the ideal rotation radius of the disk.

The position vectors of the two sensors in C_a are

$$\begin{aligned} \boldsymbol{r_1} &= (\rho_1 cos\,(\theta-\theta_1)\,,\, \rho_1 sin\,(\theta-\theta_1)) \\ \boldsymbol{r_2} &= -(\rho_2 cos\,(\theta+\theta_2)\,,\, \rho_2 sin\,(\theta+\theta_2))\,. \end{aligned} \tag{24}$$

where

$$\theta_1 = arctan\frac{-y_0}{\rho+x_0}, \theta_2 = arctan\frac{-y_0}{-\rho+x_0}. \tag{25}$$

The magnetic sensitivity vectors of the two sensors in C_a are

$$\begin{aligned} \boldsymbol{S_1} &= S_1\,(\cos\,(\theta-\theta_1)\,,\, sin\,(\theta-\theta_1)) \\ \boldsymbol{S_2} &= -S_2\,(\cos\,(\theta+\theta_2)\,,\, sin\,(\theta+\theta_2)) \end{aligned} \tag{26}$$

The combination of these two installation errors is shown in FIG. 9.

Combining (22) and (26), the magnetic sensitivity vectors are

$$\begin{aligned} \boldsymbol{S_1} &= S_1 cos\alpha_1\,(cos\,(\theta-\theta_1)\,,\, sin\,(\theta-\theta_1)) \\ \boldsymbol{S_2} &= -S_2 cos\alpha_2\,(cos\,(\theta+\theta_2)\,,\, sin\,(\theta+\theta_2))\,. \end{aligned} \tag{27}$$

The output voltage is

$$V = \boldsymbol{S_1}\cdot\boldsymbol{B_1}+\boldsymbol{S_2}\cdot\boldsymbol{B_2}+\upsilon. \tag{28}$$

In the sensor coordinate system, the voltage harmonic coefficients for the magnetic tensor components with errors can be expressed by

$$\begin{aligned} V_{2e} &\doteq \frac{1}{2}\rho\,(S_1 cos\,\alpha_1 cos\,\theta_1 + S_2 cos\,\alpha_2 cos\,\theta_2)\,(g_{xx}-g_{yy}) - \rho g_{xy} \\ &\quad\times\left[S_1 cos\,\alpha_1 sin\,\theta_1 - \frac{1}{2}S_2 cos\,\alpha_2\,(sin\,\theta_2 + sin\,(2\theta_2))\right] \end{aligned} \tag{29}$$

$$\begin{aligned} V_{2o} &\doteq \frac{1}{2}\rho\,(S_1 cos\,\alpha_1 sin\,\theta_1 - S_2 cos\,\alpha_2 sin\,\theta_2)\,(g_{xx}-g_{yy}) + \rho g_{xy} \\ &\quad\times\left[S_1 cos\alpha_1 cos\theta_1 + \frac{1}{2}S_2 cos\alpha_2\,(cos\theta_2 + cos\,(2\theta_2))\right] \end{aligned} \tag{30}$$

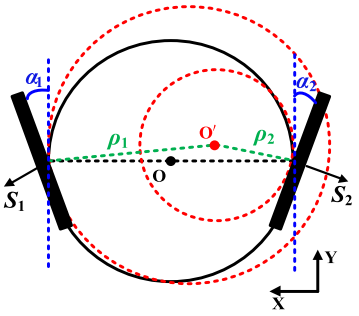

FIGURE 9. Schematic of combination of the misalignment of two sensors and offset between the rotation center and the center of the disk.

Equation (29) and (30) can be rewritten as:

$$\begin{aligned} V_{2e} &= \frac{1}{2}\rho\,(g_{xx}-g_{yy})\,R - \rho g_{xy} S \\ V_{2o} &= \rho g_{xy} T + \frac{1}{2}\rho\,(g_{xx}-g_{yy})\,U. \end{aligned} \tag{31}$$

where

$$\begin{aligned} R &= S_1 cos\,\alpha_1 cos\,\theta_1 + S_2 cos\,\alpha_2 cos\,\theta_2 \\ S &= S_1 cos\,\alpha_1 sin\,\theta_1 - \frac{1}{2}S_2 cos\,\alpha_2\,(sin\,\theta_2 + sin\,(2\theta_2)) \\ T &= S_1 cos\,\alpha_1 cos\,\theta_1 + \frac{1}{2}S_2 cos\,\alpha_2\,(cos\,\theta_2 + cos\,(2\theta_2)) \\ U &= S_1 cos\,\alpha_1 sin\,\theta_1 - S_2 cos\,\alpha_2 sin\,\theta_2 \end{aligned}$$

3) FOR DATA EXTRACTION

Let g^i_{xx}, g^i_{yy}, $and g^i_{xy}$ (i = 1, 2, and 3) be the magnetic tensor components in a three axes coordinate system C^i, and g_{xx}, g_{yy}, and g_{xy} be the magnetic tensor components in the instrument coordinate system C.

$$\boldsymbol{G}_{si} = \boldsymbol{R}_i \boldsymbol{G}_I \boldsymbol{R}_i^T, \boldsymbol{R}_i = \boldsymbol{U}\boldsymbol{Q}\boldsymbol{F}_i. \tag{32}$$

where i = 1, 2, and 3.

$\boldsymbol{G}_{s1}$, $\boldsymbol{G}_{s2}$, and $\boldsymbol{G}_{s3}$ represent three magnetic gradient tensors in the C^i system obtained by rotating the sensor system to angles of 0°, 120°, and 240° about the instrument Z-axis. $\boldsymbol{G}_I$ represents the tensor in the C^i system. $\boldsymbol{F}$, $\boldsymbol{Q}$, and $\boldsymbol{U}$ represent rotation matrixes which are formed by the Z-X-Z' rotation order with the rotation angles φ_i, λ, and ψ respectively.

$$\boldsymbol{G}_{\mathrm{I}} = \begin{bmatrix} g_{xx} & g_{xy} & g_{xz} \\ g_{xy} & g_{yy} & g_{yz} \\ g_{xz} & g_{yz} & g_{zz} \end{bmatrix}, \quad \boldsymbol{G}_{si} = \begin{bmatrix} g^i_{xx} & g^i_{xy} & g^i_{xz} \\ g^i_{xy} & g^i_{yy} & g^i_{yz} \\ g^i_{xz} & g^i_{yz} & g^i_{zz} \end{bmatrix} \tag{33}$$

$$\boldsymbol{F}_i = \begin{bmatrix} cos\varphi_i & sin\varphi_i & 0 \\ -sin\varphi_i & cos\varphi_i & 0 \\ 0 & 0 & 1 \end{bmatrix}$$

$$\boldsymbol{Q} = \begin{bmatrix} cos\lambda & 0 & -sin\lambda \\ 0 & 1 & 0 \\ sin\lambda & 0 & cos\lambda \end{bmatrix}$$

$$\boldsymbol{U} = \begin{bmatrix} cos\psi & sin\psi & 0 \\ -sin\psi & cos\psi & 0 \\ 0 & 0 & 1 \end{bmatrix}. \tag{34}$$

where $\varphi_1 = 0°$, $\varphi_2 = 120°$, $\varphi_3 = 240°$, and $\lambda = 35.2°$. ψ represent the angle between the 0° output of the shaft encoder used to determine the angle of the rotating sensor pair with respect to the system's Z' axis, see FIG 2.

To include the contribution of the error in these angles, the coordinate transformation matrixes can be re-expressed as

$$\begin{aligned}
\boldsymbol{F}_i &= \begin{bmatrix} cos\,(\varphi_i+\Delta\varepsilon_i) & sin\,(\varphi_i+\Delta\varepsilon_i) & 0 \\ -sin\,(\varphi_i+\Delta\varepsilon_i) & cos\,(\varphi_i+\Delta\varepsilon_i) & 0 \\ 0 & 0 & 1 \end{bmatrix} \\
\boldsymbol{Q} &= \begin{bmatrix} cos\,(\lambda+\Delta\lambda) & 0 & -sin\,(\lambda+\Delta\lambda) \\ 0 & 1 & 0 \\ sin\,(\lambda+\Delta\lambda) & 0 & cos\,(\lambda+\Delta\lambda) \end{bmatrix} \\
\boldsymbol{U} &= \begin{bmatrix} cos\,(\psi+\Delta\psi) & sin\psi\,(\psi+\Delta\psi) & 0 \\ -sin\,(\psi+\Delta\psi) & cos\psi\,(\psi+\Delta\psi) & 0 \\ 0 & 0 & 1 \end{bmatrix}. \qquad (35)
\end{aligned}$$

The variation in these angles is not expected to exceed (say) 1° in which case, the non-linear trigonometric function can be reasonably linearized by a Taylor series expansion.

$$\begin{aligned}
\cos(x+\Delta x) &\doteqdot \cos x + cos'x\cdot\Delta x = \cos x - sinx\cdot\Delta x \\
\sin(x+\Delta x) &\doteqdot \sin x + sin'x\cdot\Delta x = \sin x + cosx\cdot\Delta x.
\end{aligned} \qquad (36)$$

Therefore, the trigonometric functions in the three coordinate transformation matrices can be expressed by

$$\begin{aligned}
&\cos(\varphi_i+\Delta\varepsilon_i) \doteqdot p_i - q_i\Delta\varepsilon_i, \sin(\varphi_i+\Delta\varepsilon_i) \doteqdot q_i + p_i\Delta\varepsilon_i, \\
&\cos(\lambda+\Delta\lambda) \doteqdot a - b\Delta\lambda, \sin(\lambda+\Delta\lambda) \doteqdot b + a\Delta\lambda, \\
&\cos(\psi+\Delta\psi) \doteqdot c - d\Delta\psi, \sin(\psi+\Delta\psi) \doteqdot d + c\Delta\psi
\end{aligned} \qquad (37)$$

The combined coordinate transformation matrix between the sensor coordinate system and the instrument coordinate system is

$$\boldsymbol{R}_i = \begin{bmatrix} P_iAC - Q_iD & P_iD + Q_iAC & -BC \\ -P_iAD - Q_iC & P_iC - Q_iAD & BD \\ P_iB & Q_iB & A \end{bmatrix} \qquad (38)$$

where

$$\begin{aligned}
&P_i = p_i - q_i\Delta\varepsilon_i, \quad Q_i = q_i + p_i\Delta\varepsilon_i,\ A = a - b\Delta\lambda \\
&B = b + a\Delta\lambda.C = c - d\Delta\psi, \quad D = d + c\Delta\psi.
\end{aligned}$$

The tensor components in C^i system can be expressed by the tensor components in C system

$$\begin{aligned}
g^i_{xx} &= (Q_iD - AP_iC)^2 g_{xx} + 2(AP_iC - Q_iD) \\
&\quad \times (P_iD + AQ_iC) g_{xy} \\
&\quad + 2BC(AP_iC - Q_iD) g_{xz} \\
&\quad + (P_iD + AQ_iC)^2 g_{yy} - 2BC(P_iD + AQ_iC) g_{yz} \\
&\quad + B^2C^2 g_{zz} \qquad (39) \\
g^i_{xy} &= (DAP_i + CQ_i)(Q_iD - AP_iC) g_{xx} \\
&\quad + [(DQ_iA - CP_i)(Q_iD - AP_iC) \\
&\quad - (DAP_i + CQ_i)(P_iD + AQ_iC)] g_{xy} \\
&\quad + \left[DB(Q_iD + 2AP_iC) + C^2Q_iB\right] g_{xz} \\
&\quad + (DAQ_i - CP_i)(P_iD + AQ_iC) g_{yy} \\
&\quad + \left[DB(P_iD + 2AQ_iC) - C^2P_iB\right] g_{yz} - DB^2C g_{zz} \qquad (40) \\
g^i_{yy} &= (DAP_i - CQ_i)^2 g_{xx} + 2(DAQ_i - CP_i)(DAP_i + CQ_i) g_{xy} \\
&\quad - 2BD(CQ_i - AP_iD) g_{xz} \\
&\quad + (DAQ_i - CP_i)^2 g_{yy} + 2BD(CP_i - DAQ_i) g_{yz} \\
&\quad + B^2D^2 g_{zz}. \qquad (41)
\end{aligned}$$

Equations (39), (40), and (41), the tensor components and their differences can be rewritten as follows:

$$\begin{aligned}
g^i_{xx} - g^i_{yy} &= M_{1i}g_{xx} + M_{2i}g_{xy} + M_{3i}g_{xz} \\
&\quad + M_{4i}g_{yy} + M_{5i}g_{yz} + M_{6i}g_{zz} \\
g^i_{xy} &= N_{1i}g_{xx} + N_{2i}g_{xy} + N_{3i}g_{xz} \\
&\quad + N_{4i}g_{yy} + N_{5i}g_{yz} + N_{6i}g_{zz}. \qquad (42)
\end{aligned}$$

where M_{mi} and N_{ni} represent coefficients in front of the tensor components and their differences in the C system.

Combining (31) and (42), the error model of the rotating magnetic tensor gradiometer can be expressed by

$$\begin{bmatrix} V_{2e}(1) \\ V_{2o}(1) \\ V_{2e}(2) \\ V_{2o}(2) \\ V_{2e}(3) \\ V_{2o}(3) \end{bmatrix} = \boldsymbol{\Gamma}_1\boldsymbol{\Gamma}_2 \begin{bmatrix} g_{xx} \\ g_{xy} \\ g_{xz} \\ g_{yy} \\ g_{yz} \\ g_{zz} \end{bmatrix}. \qquad (43)$$

where $V_{2e}(i)$ and $V_{2o}(i)$ represent the voltage harmonic coefficients V_{2e} and V_{2o} measured in the ith sensor coordinate system and

$$\boldsymbol{\Gamma}_1 = \begin{bmatrix} \frac{1}{2}\rho & 0 & 0 & 0 & 0 & 0 \\ 0 & \rho & 0 & 0 & 0 & 0 \\ 0 & 0 & \frac{1}{2}\rho & 0 & 0 & 0 \\ 0 & 0 & 0 & \rho & 0 & 0 \\ 0 & 0 & 0 & 0 & \frac{1}{2}\rho & 0 \\ 0 & 0 & 0 & 0 & 0 & \rho \end{bmatrix}$$

$$\boldsymbol{\Gamma}_2 = \begin{bmatrix} a_{11}b_{11} & a_{21}b_{21} & a_{31}b_{31} & a_{41}b_{41} & a_{51}b_{51} & a_{61}b_{61} \\ b_{11}a_{11} & b_{21}a_{21} & b_{31}a_{31} & b_{41}a_{41} & b_{51}a_{51} & b_{61}a_{61} \\ a_{12}b_{12} & a_{22}b_{22} & a_{32}b_{32} & a_{42}b_{42} & a_{52}b_{52} & a_{62}b_{62} \\ b_{12}a_{12} & b_{22}a_{22} & b_{32}a_{32} & b_{42}a_{42} & b_{52}a_{52} & b_{62}a_{62} \\ a_{13}b_{13} & a_{23}b_{23} & a_{33}b_{33} & a_{43}b_{43} & a_{53}b_{53} & a_{63}b_{63} \\ b_{13}a_{13} & b_{23}a_{23} & b_{33}a_{33} & b_{43}a_{43} & b_{53}a_{53} & b_{63}a_{63} \end{bmatrix}$$

where $a_{\mathrm{m}i}b_{ni} = M_{\mathrm{m}i}R + N_{ni}S$, $b_{mi}a_{\mathrm{n}i} = N_{mi}T + M_{\mathrm{n}i}U$

V. ANALYSIS FOR MINOR ERRORS

A. ERRORS OF FINITE-LENGTH PARAMETERS AND IGNORING HIGHER-ORDER TENSORS

The signals from the two rotating sensors are sampled at regular angular increments of their rotation. The size of these increments is determined by an optical shaft encoder. Samples from a number of complete rotations are converted via a Fast Fourier Transform (FFT) into the frequency domain

to enable filtering of gradient signals from other signal components, e.g. the background field. The finite sample length and number of samples per revolution limits the spectral resolution of the FFT and thus introduces errors. The size of these errors can be reduced by averaging a number of FFTs. Provided that the signals are pre-filtered to meet the Nyquist sampling criteria, the sensor rotation rate was found experimentally to have little influence on the size of error signals. For both modelling and during experiments, the samples per revolution (SPR) was 512 and the number of revolutions included in each FFT was 64, thus the total number of samples per FFT was 32,768. Thus the FFT's spectral resolution is 1/32,768 times the rotation frequency. This provides sharp filtering of the desired signal at the second harmonic from any background signal which occurs at the fundamental frequency. The sensors were rotated at 3.90 r/s. Total time for a measurement along any one axis was 25 seconds, comprised of 16 seconds for sampling and 9 seconds for movement from one axis to the next.

Another kind of error is introduced if, when solving the second order tensor in the sensor coordinate system, the higher-order tensors are ignored.

In order to demonstrate the effect of errors caused by finite-length parameters and ignoring higher-order tensors, we calculated the relative errors of tensor magnitudes between the true value and the measured value of tensors with these two errors in simulation experiments. Tensor magnitude is often used to evaluate the whole performance of the magnetic tensor gradiometer and can be obtained by the tensor contraction $\sqrt{\sum_{i,j=x,y,z} G_{ij}^2}$.

The simulation procedure was undertaken as follows.

1) A magnetic dipole was placed near to the center of the disk and the true value of the magnetic gradient tensor at the center formed by the magnetic dipole calculated using an equation described in Sui [17], [18]. The true value of the tensor magnitude was computed by the equation of tensor contraction
2) The distributions of the magnetic field formed by the magnetic dipole was calculated. Two ideal sensors were placed in the simulated magnetic field and rotated through 512 equal angles per revolution. 64 cycles of these modelled rotations were processed using a FFT. The second harmonic in-phase and quadrature terms were used to derive the tensor components for each of the three sensor coordinate systems describe by (15) and (16). The full tensor components were obtained using the data extraction process described in FIG 3.
3) The relative error between the magnitude of the modelled measured tensor and the modelled true tensor was calculated for each simulation.

The simulation was repeated 1000 times. During these simulations the magnitude of the magnetic dipole moment was changed randomly from 10 A·m^2 to 10 000 A·m^2 corresponding to the range of expected moments for ore bodies containing magnetite with different concentrations and grain sizes. The direction of the magnetic dipole moment, with respect to the overall system's Z-axis, was varied randomly through a range of ± 180° in both the inclination and declination angles. The simulation results for the relative errors of the measured tensor magnitudes with respect to the actual tensor magnitudes are shown in FIG. 10.

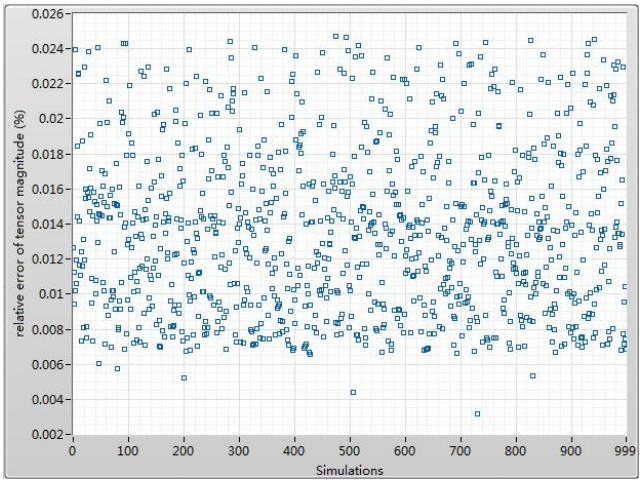

FIGURE 10. The modelled relative errors of tensor magnitudes are small when changing the magnitudes and directions of the magnetic dipole moment.

The maximum relative error is less than 0.025%, which proves that the combined errors, caused by the finite sample length and from ignoring the higher-order tensors, are very small and can be ignored.

B. ERROR OF THE DEVIATION OF THE ROTATION AXIS FROM IDEAL

Theoretically, when the measurement system rotates about the Z-axis through the angles 0°, 120° and 240°, the origins of three sensor system coordinates should coincide at a single point O, as shown in FIG. 11(a). However, because any practical rotation mechanism will be non-ideal, the three origins will be displaced from the Z-axis, as is depicted by the red lines in FIGs 11 (a) and 11 (b).

According to equation (5), if the application satisfies the condition of ignoring higher order tensors when calculating the second-order tensor, the second-order tensor will be constant around the rotation center. Therefore, the error caused by the deviation of the actual Z-axis is very small and can be ignored.

C. THE TEMPERATURE CO-EFFICIENT OF THE FLUXGATES' SIGNAL

The scaling of a fluxgate's output is to some extent temperature sensitive. This variability in sensitivity is due to temperature induce changes in the magnetic permeability of the fluxgate's core material [19]. For example, for the Bartington Mag612 fluxgate, the stated temperature coefficient of scale factor is 0.007% of full scale /°C. The normal temperature gradient downhole is of the order 3 °C /100 m [20]. If the survey depth is 1000 meters and the full range of magnetic

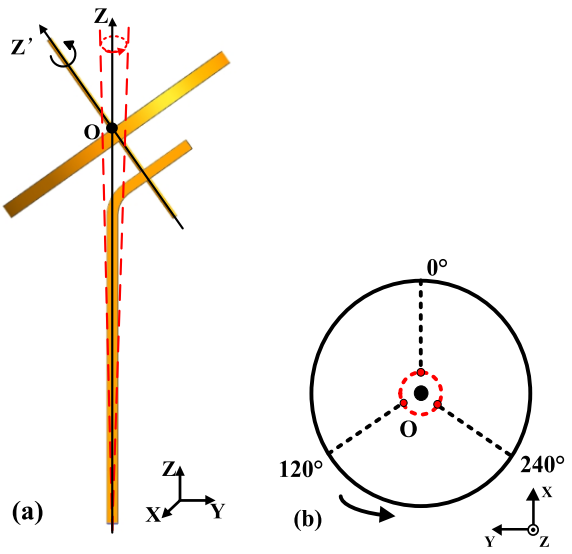

FIGURE 11. (a) Schematic of the deviation of the Z-axis. The red dashed lines represent the actual Z-axis. (b) Schematic of actual positions of three origins. The black point is the ideal position of the disk center and the red dashed circle is the actual motion of the disk center.

field is 70 000 nT, then the change of temperature can reach 30 °C and the scaling of the fluxgate can vary by up to 147 nT.

FIG 12 shows the result of an experiment that measured the temperature coefficient of two similar fluxgates over the expected temperature range of downhole operations. The plots of variation of measured field as a function of temperature show that the two fluxgates have near identical temperature coefficients with the greatest mismatch of 0.94% of the measured field about 50000 nT. The difference structure used in our downhole tensor gradiometer can reduce the influence of temperature drift effectively to introduce 0.12% error in the tensor components.

VI. INVARIANT CORRECTION OF THE DOWNHOLE MAGNETIC TENSOR GRADIOMETER

Tensor invariants are the constant quantities after the rotation of the tensor's frame of reference. Two non-zero independent invariants of the magnetic gradient tensor are:

$$I_1 = -\frac{1}{2}\sum\nolimits_{\mu,\nu=x,y,z} G_{\mu\nu}^2 \tag{44}$$

$$I_2 = |\boldsymbol{G}|\,. \tag{45}$$

Optimal correction coefficients can be obtained by using these two rotation invariants [21].

Step 1: As the second-order tensor only has 5 independent components, the error model shown in (43) can be rewritten by

$$\boldsymbol{V_m} = \begin{bmatrix} V_{2e}\,(1) \\ V_{2o}\,(1) \\ V_{2e}\,(2) \\ V_{2o}\,(2) \\ V_{2e}\,(3) \end{bmatrix} = \boldsymbol{\Gamma}_1'\boldsymbol{\Gamma}_2' \begin{bmatrix} g_{xx} \\ g_{xy} \\ g_{xz} \\ g_{yy} \\ g_{yz} \end{bmatrix} = \boldsymbol{K}\boldsymbol{G_t} \tag{46}$$

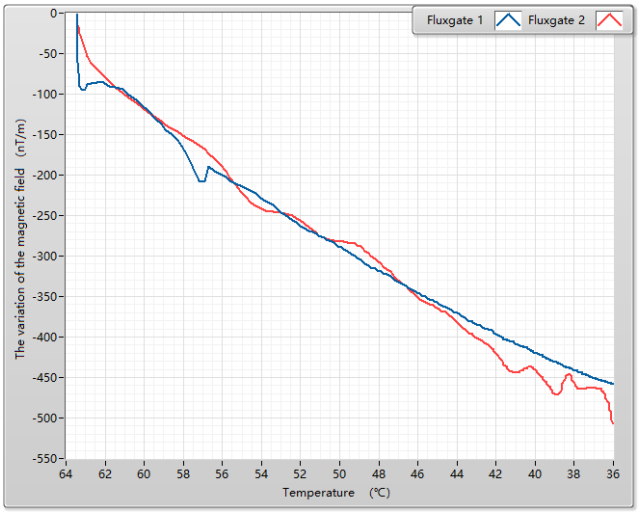

FIGURE 12. The variation of the measurements of two fluxgates with the magnetic field of 54183 nT and the temperature varies from 63 °C to 36 °C.

where $\boldsymbol{\Gamma}_1'$ and $\boldsymbol{\Gamma}_2'$ are 5∗5 sub-matrixes of $\boldsymbol{\Gamma}_1$ and $\boldsymbol{\Gamma}_2$. $\boldsymbol{V_m} = (V_{2e}(1), V_{2o}(1), V_{2e}(2), V_{2o}(2), V_{2e}(3))^{\mathrm{T}}$, $\boldsymbol{G_t} = (g_{xx}, g_{xy}, g_{xz}, g_{yy}, g_{yz})^{\mathrm{T}}$.

The invariant calibration method needs the error matrix $\boldsymbol{K}$ to be an approximate unit matrix, so we transform it into approximate unit matrix by using elementary row operations and thus (46) can be re-expressed as

$$\boldsymbol{V_u} = \boldsymbol{K_u}\boldsymbol{G_t}. \tag{47}$$

Then the correction model is

$$\boldsymbol{G_t} = \boldsymbol{K_u}^{-1}\boldsymbol{V_u} = \boldsymbol{H}\boldsymbol{V_u}. \tag{48}$$

where $\boldsymbol{K_u}$ is the error matrix, $\boldsymbol{H}$ is the reverse matrix of $\boldsymbol{K_u}$. There are 25 coefficients in $\boldsymbol{H}$, denoted as h_{ij}.

Step 2: Obtain the correction coefficients by using the property of two invariants and the least squares method [22]. Then the corrected tensor value can be calculated by (48).

VII. SIMULATIONS AND EXPERIMENTS

A. SIMULATION OF A SURVEY IN A BOREHOLE

For the purpose of simulation, take a magnetic dipole whose magnetic moment vector is (250 000, 250 000, -353 553.39) A·m^2 as a survey target located 50 meters under the ground. This dipole is equivalent to the moment of a typical cubic magnetite deposit of size 40 m × 40 m × 10 m, concentration of 52%, grain size of 20 μm and thermoremanent magnetization of 60 A/m. Simulate a vertical survey path with the closest point of approach (CPA) to the source being 15 meters, as shown in FIG. 13. For each simulated 100-meter survey line, 2000 observation points were calculated.

The procedure of simulation of a survey was as follows.

1) Compute the true value of the magnetic gradient tensors on the survey line formed by the magnetic dipole.

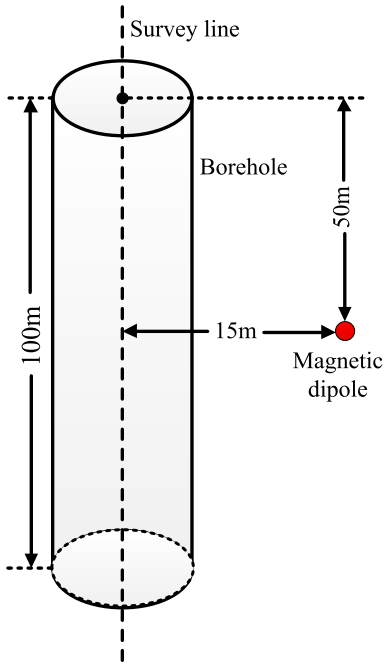

FIGURE 13. Schematic of a simulated downhole survey with a CPA to a magnetic dipole of 15 m.

TABLE 1. Error matrix.

1.10139	0.0268861	0.00094316	-0.0606255	0.0144714
0.151364	0.993667	0.000771753	0.0109846	0.00279777
-0.079472	-0.016748	1.00106	-0.0497176	0.00897122
-0.147315	0.0163352	-0.00208661	1.03218	-0.0122429
-0.58099	0.0178736	-0.00298503	0.0988806	1.07881

2) Compute the measurements of the magnetic gradient tensors by the combination of true value and error coefficients determined by the range of actual errors.
3) Obtain the correction coefficients by the tensor invariant correction method and apply them to correct the measurements on the survey line.
4) Repeat the process for 2000 discrete points along the simulated survey.
5) To provide an estimate of the effect of the error coefficients, repeat the simulated survey 1000 times using different error coefficients.

An example of a single simulated survey follows. For this example, the parameters were:

$\theta_1 = 0.625429°, \theta_2 = -1.17968°, \alpha_1 = -2.34883°, \alpha_2 = -0.190553°, \Delta\varepsilon_1 = -0.543473°, \Delta\varepsilon_2 = 0.340307°, \Delta\varepsilon_3 = 0.345963°, \Delta\psi = -0.973129°, \Delta\lambda = -0.0852217°, S_1 = 1.00372, S_2 = 0.995143.$

Using equations (43), (46) and (47), the error matrix $\boldsymbol{K_u}$ is formed by the propagation of error and elementary row operations, shown in TABLE 1:

Correction matrix $\boldsymbol{H_c}$ obtained by the tensor invariant correction method from the modelled measurements is shown in TABLE 2:

Actual correction matrix $\boldsymbol{H}$ calculated from the modelled true tensor is shown in TABLE 3:

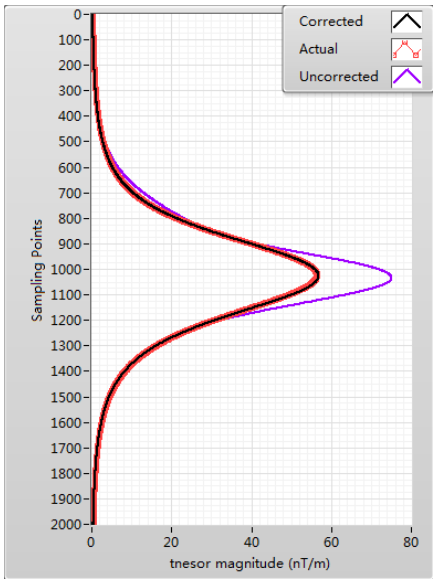

FIGURE 14. Comparison of the actual (red line with circle markers), corrected (black line with point markers), and uncorrected (purple line with point markers) tensor magnitudes of 2000 observation points on the survey line.

TABLE 2. Calculated correction matrix.

0.917604	-0.0497784	0.0301483	0.0569552	-0.012137
-0.123807	1.00963	0.0288301	-0.030166	0.012454
0.0399157	-0.013687	0.997943	0.0378642	-0.020177
0.162394	0.00237034	0.00275141	0.970604	0.0632319
0.448511	-0.0427511	0.013456	-0.117178	0.91783

TABLE 3. Actual correction matrix.

0.912638	-0.025402	-0.000760	0.054944	-0.0115466
-0.141962	1.01053	-0.0006877	-0.0190368	-0.0009267
0.0726346	0.0141558	0.998946	0.0530674	-0.0087159
0.138357	-0.019928	0.00194776	0.976369	0.00925988
0.48137	-0.028557	0.00218753	-0.0594389	0.919871

The mean square root error (RMSE) between the actual correction matrix and the calculated correction matrix is 0.0308.

FIG. 14 shows the comparison of the actual, corrected, and uncorrected tensor magnitudes of 2000 observation points on the survey line.

FIG. 15 shows the comparison of the actual, corrected, and uncorrected tensor component g_{zz} of 2000 observation points on the survey line. The results for other tensor components are similar.

As shown in FIGs. 14 and 15, the corrected tensor components and tensor magnitudes are much closer to the actual value than the uncorrected value. RMSE of relative errors of observation points on the survey line is reduced from 16.943% to 0.788% after the correction and the improvement ratio is 21.504.

B. PERFORMANCE ASSESSMENT

In order to assess the performance of the correction method, the simulation of a survey line was repeated 1000 times

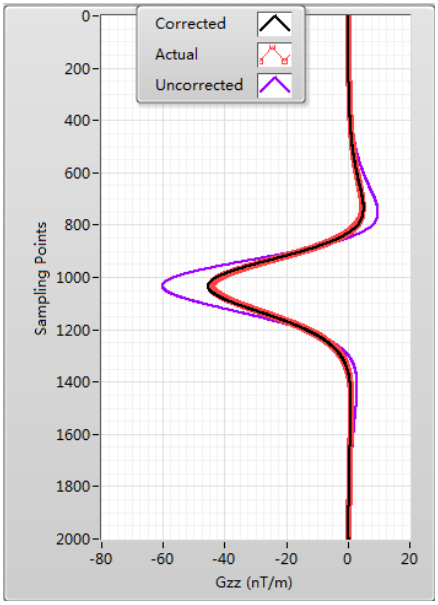

FIGURE 15. Comparison of the actual, corrected, and uncorrected tensor component g_{zz} of 2000 observation points on the survey line.

TABLE 4. Error coefficients in 1000 simulations.

For errors	Simulation coefficients
Scale factor error	Uniform distribution with amplitude of 0.01
Installation error	Uniform distribution with amplitude of 3°
Data extraction	Uniform distribution with amplitude of 1°

and all error coefficients were randomly varied according to Table 4. The error coefficients keep constant in each line and randomly varied in different lines

The RMSEs between the actual correction matrixes and the calculated correction matrixes in 1000 simulations are shown in FIG. 16. The average RMSE is 0.06 and the maximum RMSE is 0.17, which means the calculated correction matrixes are very close to the actual correction matrixes.

RMSEs of the relative errors between the actual, the corrected and the uncorrected tensor magnitudes are shown in FIG. 17. Before correction, the average RMSE of the relative error is 10% and the maximum value can reach 31%. After correction, the average RMSE of the relative error is 1% and the maximum value is reduced to 3%.

C. FIELD EXPERIMENTS

In order to verify the effectiveness of the calibration method, we designed an experiment to check tensor corrections as a function of orientation of the rotating gradiometer while measuring a fixed magnitude, gradient tensor. For this experiment, a replica of the CSIRO gradiometer was built at Jilin University. The chosen fluxgate sensors have noise characteristics of 10 pT at 1Hz and physical dimensions of length 30 mm and outside diameter (O.D.) of 7 mm. These two fluxgates were placed parallel to each other on a 77 mm diameter disk with a separation $(\rho_1 + \rho_2)$ of 60 mm. The rotating gradiometer was fitted into a downhole probe of length 1450 mm long and O.D. of 88 mm.

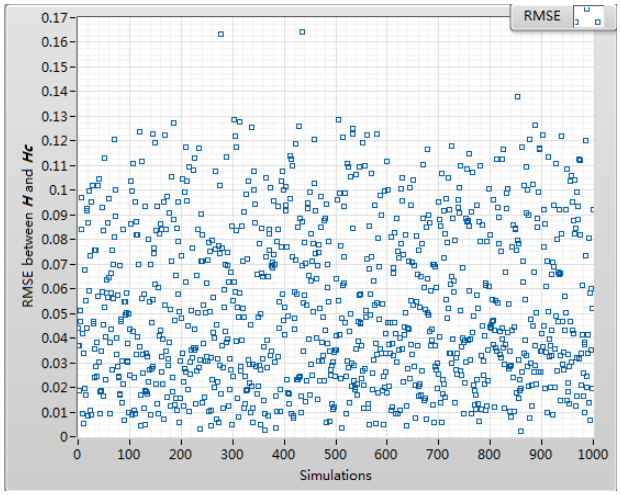

FIGURE 16. RMSEs between the actual correction matrix and the calculated correction matrix in 1000 simulations.

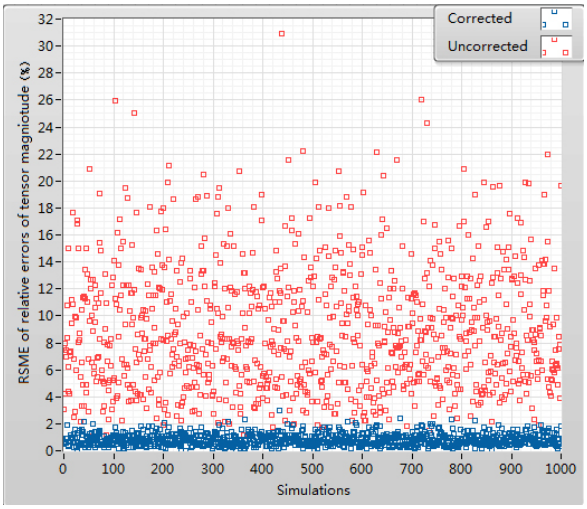

FIGURE 17. RMSEs of the relative errors between the actual, the corrected and the uncorrected tensor magnitudes in the 1000 simulations.

We placed a small magnet, with a magnetic moment of 0.375 A·m^2, in an area of uniform magnetic field to provide a constant magnetic gradient at a fixed distance between the magnet and gradiometer. The tensor gradiometer was mounted on a simple two-axis, non-magnetic mount which allowed it to be rotated about a fixed point (the disk center), see FIG. 18. The distance between the small magnet and the fixed point was 67 cm. The extent of possible angular movement of the gradiometer around the center of rotation was 360° around the vertical axis and approximately 270° around the horizontal axis, i.e. conceptually about three-quarters of a sphere.

Tensor measurements were made for 82 orientations of the gradiometer with these varying orientations arranged to uniformly cover the accessible surface of the sphere. Tensor corrections coefficients were calculated for each orientation of the gradiometer and the effectiveness of the applied correction evaluated by calculating the ratio of the tensor magnitude before correction to that after correction.

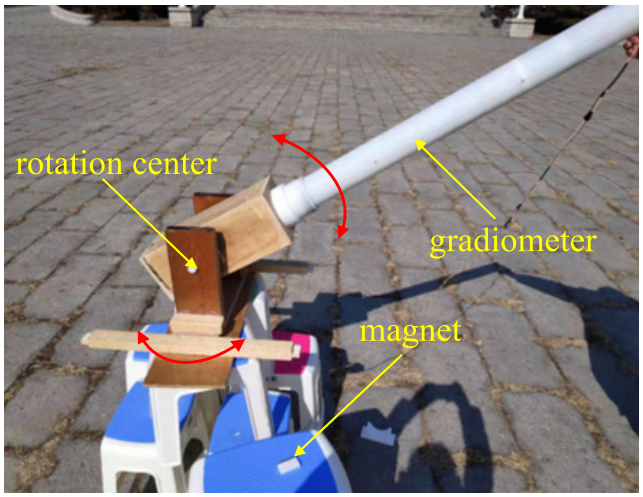

FIGURE 18. Photograph of the field experiment for rotation correction.

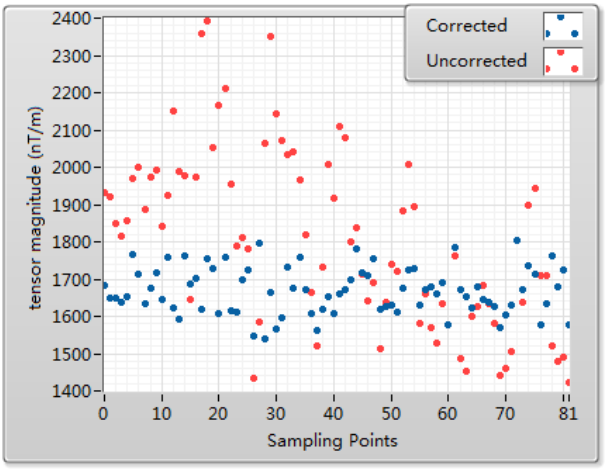

FIGURE 19. Comparison of the corrected and uncorrected tensor magnitudes for the rotation correction experiment.

TABLE 5. Correction matrix.

0.672679	-0.0189783	0.0604618	-0.685502	-0.376368
-0.0852696	1.05844	0.122994	-0.106015	0.013492
-0.0534042	-0.0366545	0.801367	0.0220875	0.236196
0.12119	0.360568	0.158183	0.919653	0.113466
0.247412	0.00686036	-0.107625	0.110264	0.82219

Comparison of the 82 tensor magnitudes before and after correction is shown in FIG. 19.

The correction matrix $\boldsymbol{H_c}$ of the experiment is shown in TABLE 5.

The standard deviations of tensor magnitudes are 233.27 nT/m and 62.33 nT/m before and after correction respectively.

We have observed that the calibration method does improve the calculated tensor components. However, the corrections are not as effective as for the simulated results. Some suggested reasons for this reduced effectiveness are: Firstly, the center of the gradiometer sensor was located approximately 3 cm above the fixed point in the mount, thus the gradiometer did not rotate about its center and so the distance between this center and the magnet varied. Secondly, magnetic field measurements made using an Overhauser magnetometer showed that the background field was non-uniform. The measurement site has a total vertical gradient of 20 nT/m. As a result, the actual measured tensor values differed significantly from the simulated values, and thus the actual correction improvement ratio could not match the simulated results.

VIII. CONCLUSION

The proposed use of two independent tensor rotation invariants to provide corrections for errors associated with the non-ideal mechanical construction of a rotating gradiometer was investigated both via simulation and experimentally. The simulation results indicate that it is possible to use the proposed method to obtain significant improvement in the accuracy of the measured tensor components. Our experimental results showed some improvement in accuracy thus confirming the potential value of the method. The error analysis and correction method is not dependent on the type of vector magnetometer used to construct the rotating gradiometer. Rotation correction experiments can be further improved from the following two aspects. The first is to search a uniform gradient field that meets our experimental requirements, the second is to improve the experimental rotation holder to ensure that the distance between magnet and gradiometer is fixed.

REFERENCES

[1] M. Schiffler, M. Queitsch, M. Schneider, R. Stolz, W. Krech, H. G. Meyer, and N. Kukowski, "Calculation and analysis of magnetic gradient tensor components of global magnetic models," in *Proc. AGU Fall Meeting Abstr.*, San Francisco, CA, USA, vol. 1. 2014, p. 3.

[2] K. Leslie, C. A. Foss, D. Hillan, and K. Blay, "A downhole magnetic tensor gradiometer for developing robust magnetisation models from magnetic anomalies," in *Proc. Iron Ore*, 2015, pp. 1–11.

[3] R. J. Blakely, "Potential theory in gravity and magnetic applications," in *Plastics*, 2nd ed. New York, NY, USA: Cambridge Univ. Press, 1996, p. 115.

[4] C. A. Foss, K. Leslie, and D. Hillan, "Detection of the structural dip of a magnetic sheet from analysis of borehole magnetic gradient tensor data," in *Proc. CSIRO EP*, Apr. 2016.

[5] W. Bosum, D. Eberle, and H.-J. Rehli, "A gyro-oriented 3-component borehole magnetometer for mineral prospecting, with examples of its application," *Geophys. Prospecting*, vol. 36, no. 8, pp. 933–961, Nov. 1988.

[6] G. Li, "Study on airborne fluxgate magnetic tensor gradiometer," M.S. thesis, College Instrum. Elect. Eng., Jilin Univ., Changchun, China, 2013.

[7] L. B. Pedersen and T. M. Rasmussen, "The gradient tensor of potential field anomalies: Some implications on data collection and data processing of maps," *Geophysics*, vol. 55, no. 12, pp. 1558–1566, 1990, doi: 10.1190/1.1442807.

[8] C. A. Foss, "Improvements in source resolution that can be expected from inversion of magnetic field tensor data," *Lead. Edge*, vol. 25, no. 1, pp. 81–84, Jan. 2006.

[9] S. Ehmann, A. Hördt, M. Leven, and C. Virgil, "Paleomagnetic inclination and declination from three-component borehole magnetometer data—New insights from logging in the Louisville seamounts," *J. Geophys. Res. Solid Earth*, vol. 120, pp. 18–41, Jan. 2014, doi: 10.1002/2014JB011531.

[10] P. W. Schmidt and D. A. Clark, "The magnetic gradient tensor: Its properties and uses in source characterization," *Lead. Edge*, vol. 25, no. 1, pp. 75–78 Jan. 2006, doi: 10.1190/1.2164759.

[11] Y. Y. Sui and G. Li, "Compact fluxgate magnetic full-tensor gradiometer with spherical feedback coil," *Rev. Sci. Instrum.*, vol. 85, no. 1, 2014, Art. no. 014701, doi: 10.1063/1.4856675.

[12] R. Stolz, V. Zakosarenko, M. Schulz, A. Chwala, L. Fritzsch, H. G. Meyer, and E. O. Köstlin, "Magnetic full-tensor SQUID gradiometer system for geophysical applications," *Lead. Edge*, vol. 25, no. 2, pp. 178–180, Feb. 2006, doi: 10.1190/1.2172308.

[13] D. L. Tilbrook, "Rotating magnetic tensor gradiometry and a superconducting implementation," *Supercond. Sci. Technol.*, vol. 22, no. 7, pp. 1–7, Jun. 2009, doi: 10.1088/0953-2048/22/7/075002.
[14] A. Sunderland, L. Ju, D. G. Blair, W. McRae, and A. V. Veryaskin, "Optimizing a direct string magnetic gradiometer for geophysical exploration," *Rev. Sci. Instrum.*, vol. 80, Oct. 2009, Art. no. 104705, doi: 10.1063/1.3227237.
[15] M. Schiffler, M. Queitsch, R. Stolz, A. Chwala, W. Krech, H. G. Meyer, and N. Kukowski, "Calibration of SQUID vector magnetometers in full tensor gradiometry systems," *Geophys. J. Int.*, vol. 198, no. 2, pp. 954–964, 2014, doi: 10.1093/gji/ggu173.
[16] P. Schmidt, D. Clark, K. Leslie, M. Bick, D. Tilbrook, and C. Foley, "GETMAG—A SQUID magnetic tensor gradiometer for mineral and oil exploration," *Explor. Geophys.*, vol. 35, no. 4, pp. 297–305, Jan. 2004, doi: 10.1071/EG04297.
[17] Y. Y. Sui, K. Leslie, and D. Clark, "Multiple-order magnetic gradient tensors for localization of a magnetic dipole," *IEEE Magn. Lett.*, vol. 8, Feb. 2017, Art. no. 6506605, doi: 10.1109/LMAG.2017.2708682.
[18] Y. Sui, P. Kang, D. Cheng, and J. Lin, "Analysis and simulation of flight effects on an airborne magnetic gradient tensor measurement system," *IEEE Trans. Instrum. Meas.*, vol. 64, no. 10, pp. 2657–2665, Oct. 2015, doi: 10.1109/TIM.2015.2420377.
[19] K. K. Qi, C. Shi, and B. Lü, "Study on temperature characteristic of fluxgate sensor detectors," *Chin. J. Sens. Actuators*, vol. 27, no. 11, pp. 1636–1641, Nov. 2014.
[20] I. B. Fridleifsson, R. Bertani, and E. Huenges, "The possible role and contribution of geothermal energy to the mitigation of climate change," in *Proc. IPCC Scoping Meeting Renew. Energy Sour.*, Luebeck, Germany, 2008, vol. 20, no. 25, pp. 59–80.
[21] Y. Sui, S. Liu, Z. Zhou, Y. Wang, and D. Cheng, "Invariant Calibration of Magnetic Tensor Gradiometers," *IEEE Magn. Lett.*, vol. 8, Jan. 2017, Art. no. 6505105, doi: 10.1109/LMAG.2017.2677381.
[22] G. Yin, Z. Yingtang, F. Hongbo, R. Guoquan, and L. Zhining, "One-step calibration of magnetic gradient tensor system with nonlinear least square method," *Sens. Actuators A, Phys.*, vol. 229, pp. 77–85, Jun. 2015, doi: 10.1016/j.sna.2015.03.026.

YANGYI SUI (M'18) received the B.Eng., M.S., and Ph.D. degrees from Jilin University, Changchun, China, in 2002, 2005, and 2008, respectively.

He is currently a Professor with the College of Instrumentation and Electrical Engineering, Jilin University. His current research interests include magnetic measurement, and magnetic gradient tensor measurement systems and their applications, especially based on unmanned platforms.

WEI HE received the B.Eng. degree from Shandong University, Jinan, China, in 2016. She is currently pursuing the M.S. degree with Jilin University, Changchun, China. Her current research interests include the error correction of downhole rotating magnetic tensor gradiometer and the reorientation of magnetic field information.

ZHENGHUI XIA received the B.Eng. degree from Jilin University, Changchun, China, in 2016, where he is currently pursuing the M.S. degree in electrical engineering and automation.

His main research interest includes the development of magnetic tensor gradient systems based on rotation modulation.

SHIBIN LIU received the B.Eng. degree in electrical engineering and automation from Jilin University, Changchun, China, in 2016, where he is currently pursuing the Ph.D. degree in detection technology and automatic equipment.

His current research interests include the calibration of magnetic gradient tensor measurement systems and the inversion from magnetic gradient tensor data.

KEITH LESLIE is based in Sydney, Australia. For the past 20 years, he was involved in the field of design and implementation of magnetic gradiometers based on both superconductors and fluxgate sensors. He joined the Australian Commonwealth Scientific and Industrial Research Organisation (CSIRO), in 1974.